Research Square

Preprints are preliminary reports that have not undergone peer review.
They should not be considered conclusive, used to inform clinical practice,
or referenced by the media as validated information.

# Room-Temperature Stabilisation and Optical Band-Gap Tuning of δ-$Bi_2O_3$ Fluorite Ceramics by Nb/V/P Triple Co-substitution

**Badr BAACH**

badr.baach@uit.ac.ma

**Taoufiq Guedira**

**Research Article**

**Keywords:** δ-$Bi_2O_3$, Fluorite structure, Band-gap engineering, Urbach energy, Diffuse reflectance spectroscopy

**Posted Date:** June 2nd, 2026

**DOI:** https://doi.org/10.21203/rs.3.rs-9769862/v1

**License:** This work is licensed under a Creative Commons Attribution 4.0 International License.
Read Full License

**Additional Declarations:** No competing interests reported.

# Room-Temperature Stabilisation and Optical Band-Gap Tuning of δ-$Bi_2O_3$ Fluorite Ceramics by Nb/V/P Triple Co-substitution

**Badr Baach[1]*, Taoufiq Guedira[1].**

[1]*Organic Chemistry, Catalysis and Environment Laboratory, Faculty of Sciences, Ibn Tofail University, B.P. 133, 14000 Kenitra, Morocco.*

* Corresponding author:

**Badr Baach***

**E-mail:** baachbadr@gmail.com

**Phone:** 00212604401157

https://orcid.org/my-orcid?orcid=0000-0002-6349-2343

## Abstract

Room-temperature stabilisation and optical engineering of the δ-$Bi_2O_3$ cubic fluorite phase ($Fm\bar{3}m$) remains a key challenge for optoelectronics. We report the solid-state synthesis of $Bi_{17}Nb_{3-4x}V_{2x}P_{2x}O_{33}$ (x = 0, 0.15, 0.45, 0.525) solid solutions, where $Nb^{5+}/V^{5+}/P^{5+}$ co-substitution successfully stabilises this high-temperature structure at ambient conditions. X-ray diffraction confirms a systematic lattice contraction (from 5.556 to 5.503 Å) driven by a progressive decrease in average cation radius. Diffuse reflectance spectroscopy reveals an indirect band-gap widening from 1.76 eV to 2.18 eV, attributed primarily to enhanced O 2p/Bi 6p orbital hybridisation via lattice contraction, alongside V 3d conduction-band state contributions. Concurrently, the Urbach energy increases (280–410 meV), reflecting dopant-induced band-tail disorder, while empirical refractive indices decrease (2.82 to 2.63) due to reduced ionic polarisability. These results establish multi-cation co-doping as an effective, mechanistically interpretable strategy for tuning optoelectronic properties in bismuth oxide ceramics.

**Keywords:** δ-$Bi_2O_3$; Fluorite structure; Band-gap engineering; Urbach energy; Diffuse reflectance spectroscopy

## 1. Introduction

Bismuth oxide ($Bi_2O_3$) occupies a prominent position in materials science owing to its rich structural polymorphism and diverse functional properties, which have enabled applications in solid oxide fuel cells (SOFCs), photocatalysis, and emerging optoelectronic technologies [1–

3]. Among its polymorphs, the high-temperature cubic δ-$Bi_2O_3$ phase (fluorite-type $Fm\bar{3}m$) is particularly noteworthy for its high structural symmetry, large ionic polarisability, and exceptionally high oxygen-ion conductivity (~1 S $cm^{-1}$ at 750 °C) [1,4]. However, δ-$Bi_2O_3$ is thermodynamically stable only above approximately 730 °C and transforms spontaneously to the monoclinic α-phase upon cooling, which severely limits its exploitation at ambient conditions [1].

To overcome this limitation, considerable effort has been devoted to stabilising the fluorite structure at room temperature through cationic substitution [5, 6]. Isovalent dopants such as $Y^{3+}$, $Dy^{3+}$, and $Er^{3+}$ preserve the intrinsic oxygen-vacancy concentration of the δ-phase while modifying the local bonding environment [7, 8]. By contrast, higher-valence dopants such as $Nb^{5+}$ and $W^{6+}$ progressively fill the intrinsic anion vacancies of the fluorite framework, thereby reducing oxide-ion mobility but enhancing kinetic phase stability [7, 8]. Although rare-earth dopants are highly effective stabilisers, their elevated cost and limited natural abundance motivate the search for more economical alternatives. In this context, pentavalent transition-metal ions ($V^{5+}$) and network-forming species ($P^{5+}$) have emerged as attractive candidates owing to their strong stabilising ability and compatibility with the Bi–O framework [9, 10]. Our previous work demonstrated that Nb-based substitution successfully stabilises the fluorite phase while modifying ionic transport properties [11]. However, the influence of multi-cation co-doping on the optical and electronic structure of δ-$Bi_2O_3$ remains comparatively underexplored.

Although the structural stabilisation of δ-$Bi_2O_3$ through V and P co-doping has been reported [9, 10], a detailed characterisation of the resulting optical constants is essential for evaluating the potential of these materials in visible-light photonics and photocatalysis. Incorporation of $V^{5+}$ and $P^{5+}$ is expected not only to stabilise the cubic lattice but also to modify the electronic band structure, potentially shifting the absorption edge and altering defect-related optical transitions [12]. Furthermore, high dopant concentrations inevitably introduce structural disorder, which can be quantified through the Urbach energy ($E_u$) — a parameter characterising the exponential band-tail state distribution arising from lattice distortions and compositional fluctuations [13–16]. Despite its diagnostic value, $E_u$ is often neglected in optical studies of complex oxides.

In this context, the present work focuses on the synthesis and comprehensive optical characterisation of Nb/V/P co-doped δ-$Bi_2O_3$ ceramics with nominal composition $Bi_{17}Nb_{3-4x}V_{2x}P_{2x}O_{33}$. Beyond confirming structural stabilisation by X-ray powder diffraction

and scanning electron microscopy, we employ diffuse reflectance spectroscopy (DRS) combined with the Kubelka–Munk formalism to determine the optical band gap via Tauc analysis. We further extract the Urbach energy to quantify band-tail disorder, and estimate the static refractive index using established empirical relations, with the aim of elucidating the relationship between multi-cation substitution, structural disorder, and optoelectronic behaviour.

## 2. Experimental Procedure

### *2.1. Sample preparation*

The synthesis of the powder with the composition $Bi_{17}Nb_{3-4x}V_{2x}P_{2x}O_{33}$ (x = 0, 0.15, 0.45, 0.525) was performed using the solid-state reaction technique. A stoichiometric mixture of dried oxide powders of $Bi_2O_3$ (Riedel-De Haen, 99.9% purity), $V_2O_5$, $(NH_4)_2HPO_4$, and $Nb_2O_5$ (Riedel-De Haen, 99.9% purity) was homogenized by prolonged grinding in an agate mortar. The reaction mixture was placed in an alumina crucible and pre-heated at 350 °C overnight to decompose $(NH_4)_2HPO_4$ and eliminate $NH_3$ and $H_2O$. Two successive heat treatments were carried out at 820 °C for 15 h each, with intermediate grinding to improve reactant homogeneity. The phases were prepared according to the following reaction:

$$8.5Bi_2O_3 + (1.5 - 2x)Nb_2O_5 + xV_2O_5 + 2.\mathrm{x}(NH_4)_2HPO_4 \rightarrow Bi_{17}Nb_{3-4x}V_{2x}P_{2x}O_{33} + 4xNH_3 \uparrow + 3xH_2O \uparrow$$

The reacted powders were reground and pelletised into cylindrical pellets between successive thermal treatments.

**Table 1.** Nominal compositions for the synthesized $Bi_{17}Nb3_{-4x}V_{2x}P_{2x}O_{33}$ solid solutions.

| Composition | Compound formula |
|---|---|
| x = 0 | $Bi_{17}Nb_3O_{33}$ |
| x = 0.15 | $Bi_{17}Nb_{2.4}P_{0.3}V_{0.3}O_{33}$ |
| x = 0.45 | $Bi_{17}Nb_{1.2}P_{0.9}V_{0.9}O_{33}$ |
| x = 0.525 | $Bi_{17}Nb_{0.9}P_{1.05}V_{1.05}O_{33}$ |

### *2.2. Sample characterization*

The crystalline structure and phase purity of the synthesized powders were examined by X-ray powder diffraction (XRD) using a PANALYTICAL X'PERT POWDER diffractometer

with Cu Kα radiation (λ = 1.5406 Å). The diffraction patterns were recorded at room temperature over a 2θ range of 10° to 80° with a scan step of 0.05°. The XRD patterns were indexed using X'Pert Highscore Plus software with the ICDD database.

The surface morphology of the samples was examined using a Scanning Electron Microscope (SEM, SUPRA 40 VP GEMINI ZEISS COLUMN), coupled with an Energy Dispersive X-Ray Spectroscopy (EDX, Oxford Instruments X-Max 20 $mm^2$) analyzer.

#### *2.2.1. Lattice Parameter and Structural Parameter Determination*

The lattice parameter ($a$) of each cubic composition was determined analytically from the positions of five diffraction reflections — (111), (200), (220), (311), and (222) — identified in each pattern. The interplanar spacing $d$_hkl was calculated from the measured peak position 2θ using Bragg's law:

$$d_{hkl} = \frac{\lambda}{2sin\theta}$$

where λ = 1.54056 Å (Cu $K\alpha_1$) and θ = (2θ_measured)/2. The lattice parameter was then obtained from:

$$a = d_{hkl}\sqrt{h^2 + k^2 + l^2}$$

The reported value for each composition is the arithmetic mean of five independently calculated values; the associated uncertainty is the standard deviation. The average cation radius $\langle r \rangle$ was calculated from the nominal stoichiometry using Shannon ionic radii [17]:

$$\langle r \rangle = \frac{17r_{Bi^{3+}} + (3 - 4x)r_{Nb^{5+}} + 2xr_{P^{5+}} + 2xr_{V^{5+}}}{20}$$

where $Bi^{3+}$ = 1.17 Å (CN = 8), $Nb^{5+}$ = 0.64 Å, $V^{5+}$ = 0.54 Å, $P^{5+}$ = 0.38 Å (CN = 6 for all dopants) [17]. Since CN = 8 values are unavailable for $V^{5+}$ and $P^{5+}$, the CN = 6 values are used as the best available approximation; $\langle r \rangle$ values should therefore be interpreted as qualitative compositional trend indicators. All structural parameters are compiled in **Table 2**.

### 2.3. Optical Characterization

The optical properties were investigated using UV-Vis-NIR Diffuse Reflectance Spectroscopy (DRS). The optical diffuse reflectance spectra ($R_\infty$) were recorded at room

temperature using a JASCO V-700 UV-Vis spectrophotometer equipped with an integrating sphere. To account for scattering effects inherent to the powder samples, the raw reflectance data was converted into the equivalent absorption coefficient using the Kubelka-Munk (K-M) remission function, $F(R_\infty)$:

$$F(R_\infty) = \frac{(1 - R_\infty)^2}{R_\infty} = \frac{\alpha}{S}$$

where $R_\infty$ is the absolute reflectance, α is the absorption coefficient, and S is the scattering coefficient.

The optical band gap energy ($E_g$) was determined using the Tauc method, by plotting $[F(R_\infty)h\nu]^n$ against photon energy (hν), where n = 1/2 for indirect allowed transitions, consistent with the reported band structure of δ-$Bi_2O_3$ [18, 19]. Furthermore, the structural disorder and the density of localized states in the band tails were quantitatively assessed through the calculation of Urbach energy ($E_u$), derived from the slope of $\ln(F(R_\infty))$ versus photon energy within the lower energy region.

## 3. Results and Discussion

### 3.1. Structural and Morphological Analysis

The phase purity and crystalline integrity of the synthesised powders were assessed by X-ray powder diffraction. All reflections could be indexed to the face-centred cubic fluorite structure (space group $Fm\bar{3}m$ ), consistent with the high-temperature δ-$Bi_2O_3$ phase and related $Bi_{17}M_3O_{33}$-type compounds [20–22].

No reflections attributable to secondary phases, unreacted precursor oxides, or segregated dopant-rich regions were detected across the full 2θ range examined, noting that XRD phase detection sensitivity is typically limited to crystalline phases present at ≥2–3 wt%. The persistence of single-phase cubic symmetry across the entire composition range — from Nb-dominated (x = 0) to near-equal V/P/Nb occupancy (x = 0.525) — is noteworthy given the substantial structural demands imposed by $P^{5+}$ incorporation and underscores the robustness of the fluorite framework as a host for multi-cation substitution.

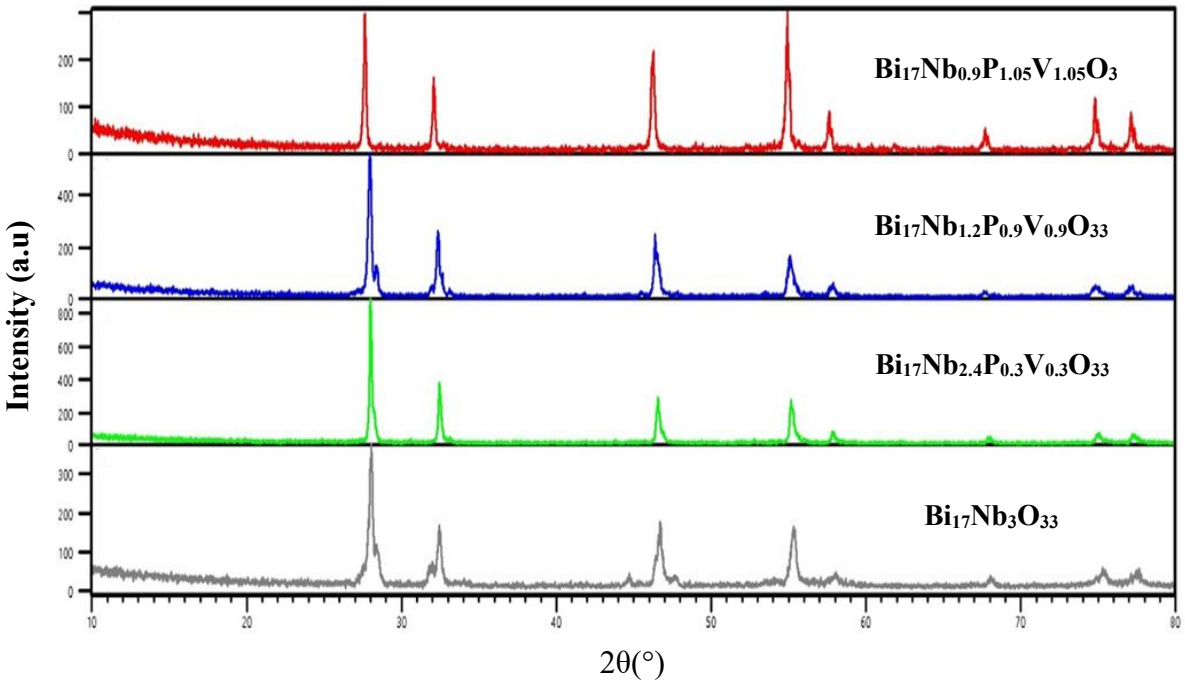



**Fig. 1**. X-ray powder diffraction (XRD) patterns of the synthesized $Bi_{17}Nb_{3-4x}V_{2x}P_{2x}O_{33}$ solid solutions at room temperature.

The main reflections observed are consistent with the face-centred cubic ($Fm\bar{3}m$) fluorite-related structure derived from δ-$Bi_2O_3$ (ICDD card no. 00-047-1057) [12, 14, 15]. For the parent composition $Bi_{17}Nb_3O_{33}$, the analytically determined lattice parameter is a = 5.556 ± 0.020 Å (**Table 2**), with principal d-spacings: d(111) ≈ 3.1 Å (2θ ≈ 28°), d(200) ≈ 2.7 Å (2θ ≈ 33°), d(220) ≈ 1.9 Å (2θ ≈ 46°), d(311) ≈ 1.6 Å (2θ ≈ 55°), and d(222) ≈ 1.6 Å (2θ ≈ 57°). The single-phase cubic nature of all compositions up to x = 0.525 confirms that the fluorite cation cage can accommodate the combined substitution of three crystallographically distinct pentavalent species without structural decomposition — a result that is not a priori guaranteed given the pronounced size mismatch of $P^{5+}$ (r = 0.38 Å for CN = 6) relative to the host $Bi^{3+}$ site.

A systematic shift of the principal fluorite reflections — most clearly observed for the (111) peak — toward higher 2θ values is observed with increasing $V^{5+}$ and $P^{5+}$ content (Fig. 1), qualitatively consistent with Vegard's law [23]. This contraction reflects a net decrease in average cation radius as $Nb^{5+}$ (0.64 Å) is progressively replaced by the smaller $V^{5+}$ (0.54 Å) and $P^{5+}$ (0.38 Å) species (CN = 6 [17]; note that CN = 8 values are unavailable for $V^{5+}$ and $P^{5+}$, making a strict crystallographic comparison approximate). It is important to note, however, that the three dopants are not crystallographically equivalent: $Nb^{5+}$ and $V^{5+}$, as transition-metal $d^0$ ions, are well-suited to the fluorite cation environment and act primarily as structural stabilisers. $P^{5+}$, by contrast, strongly prefers tetrahedral coordination in most oxide systems and therefore introduces severe local distortion when constrained to the 8-coordinate fluorite site [12]. Its role

is thus best described as that of a controlled disorder-inducing species rather than a simple size-filling substituent.

The rate of lattice contraction is expected to decelerate at higher x values, since the compositional increments in $V^{5+}$ and $P^{5+}$ become smaller relative to the total cation content, and the remaining $Nb^{5+}$ provides a stabilising structural framework. The average-structure contraction observed by XRD is therefore accompanied by increasing local structural heterogeneity — a direct structural antecedent of the progressive band-tail broadening observed optically (Section 3.2). The resulting decrease in lattice parameter introduces local strain within the fluorite cage that is expected to influence both the electronic band structure and the oxygen sublattice disorder [19, 24-25].

The lattice parameters, extracted analytically from five independent reflections for each composition and summarised in **Table 2**, decrease monotonically across the series, from a = 5.5560 ± 0.020 Å for $Bi_{17}Nb_3O_{33}$ (x = 0) to a = 5.5031 ± 0.006 Å for $Bi_{17}Nb_{0.9}P_{1.05}V_{1.05}O_{33}$ (x = 0.525), representing a total contraction of Δa = 0.0529 Å (0.95%). This contraction is accompanied by a corresponding decrease in the calculated average cation radius ⟨r⟩ from 1.0905 Å (x = 0) to 1.0737 Å (x = 0.525), confirming qualitative adherence to Vegard's law [18, 23].

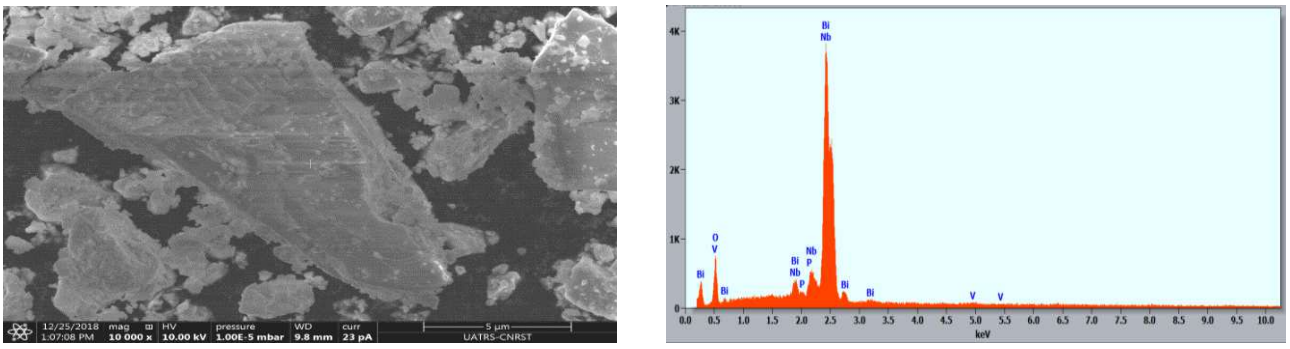
Notably, the rate of contraction is not constant across the series: the largest incremental change occurs between x = 0 and x = 0.15 (Δa = −0.0342 Å), followed by a markedly smaller step between x = 0.15 and x = 0.45 (Δa = −0.0073 Å), before recovering to −0.0114 Å between x = 0.45 and x = 0.525. This non-linear behaviour is physically consistent with partial strain compensation at intermediate compositions, where the opposing contributions of decreasing $Nb^{5+}$ content and increasing $V^{5+}/P^{5+}$ content create a near-balanced multi-cation occupancy that temporarily reduces the net rate of lattice contraction. The subsequent acceleration at x = 0.525 reflects the growing dominance of the highly mismatched $P^{5+}$ ion (r = 0.38 Å, CN = 6).

Importantly, this structural deceleration and recovery directly mirrors the non-monotonic evolution of the Urbach energy discussed in Section 3.2, providing a crystallographic basis for the observed optical behaviour and confirming that the average-structure evolution measured by XRD and the local structural disorder probed optically are complementary descriptions of the same underlying compositional transformation.

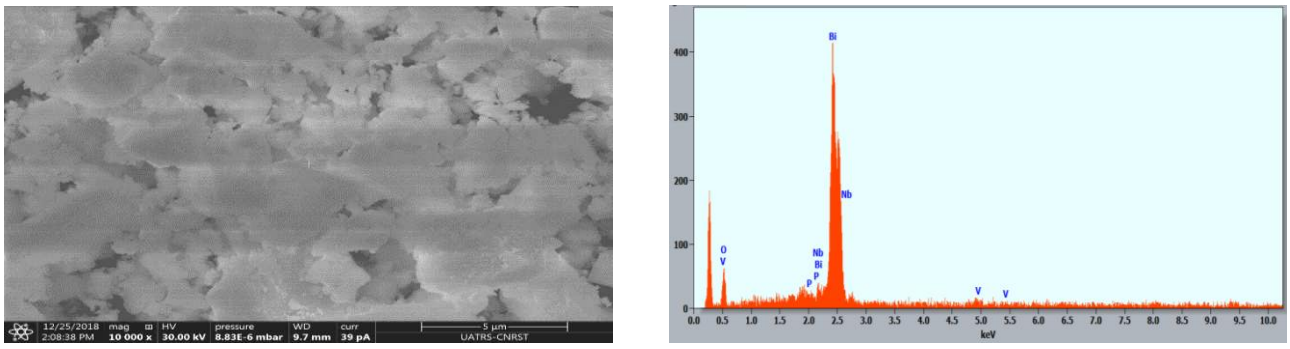
SEM micrographs (**Fig. 2**) reveal a dense, agglomerated microstructure for all compositions. The particles exhibit irregular polyhedral morphologies with evidence of grain necking and inter-particle contact area development, consistent with significant mass transport and particle coalescence during high-temperature sintering at 820 °C. The qualitative homogeneity of the microstructure across the composition series is consistent with the single-phase XRD result, suggesting that the multi-cation co-substitution does not induce large-scale phase segregation detectable by SEM. EDX spectra confirm the presence of Bi, Nb, V, P, and O in each composition, broadly consistent with the nominal stoichiometries. It should be noted that quantitative EDX analysis of P is subject to uncertainty owing to the partial spectral overlap between the P Kα emission line (2.013 keV) and the Bi Mβ line (2.044 keV); the P detection should therefore be regarded as qualitative confirmation of incorporation rather than precise quantification. The absence of discrete secondary-phase particles or compositional segregation zones in the SEM/EDX data provides supplementary evidence for solid-solution formation, complementing the XRD phase analysis.

**Table 2.** Structural parameters of $Bi_{17}Nb_{3-4x}V_{2x}P_{2x}O_{33}$ solid solutions derived from X-ray powder diffraction at room temperature.

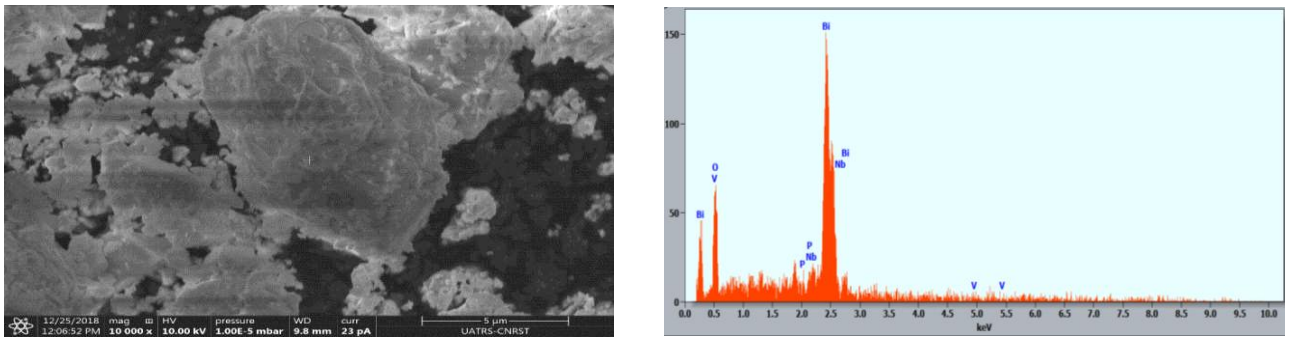
| **Parameter** | **$Bi_{17}Nb_3O_{33}$** | **$Bi_{17}Nb_{2.4}P_{0.3}V_{0.3}O_{33}$** | **$Bi_{17}Nb_{1.2}P_{0.9}V_{0.9}O_{33}$** | **$Bi_{17}Nb_{0.9}P_{1.05}V_{1.05}O_{33}$** |
|---|---|---|---|---|
| **x value** | 0 | 0.15 | 0.45 | 0.525 |
| **Space group** | $Fm\bar{3}m$ | $Fm\bar{3}m$ | $Fm\bar{3}m$ | $Fm\bar{3}m$ |
| **Structure type** | Fluorite | Fluorite | Fluorite | Fluorite |
| **a (Å)** | 5.5560 ± 0.020 | 5.5218 ± 0.010 | 5.5145 ± 0.002 | 5.5031 ± 0.006 |
| **Δa from x=0 (Å)** | - | −0.0342 | −0.0415 | −0.0529 |
| **Δa (%)** | - | −0.62% | −0.75% | −0.95% |
| **⟨r⟩_cation (Å)** | 1.0905 | 1.0851 | 1.0743 | 1.0716 |
| **Δ⟨r⟩ from x=0 (Å)** | - | −0.0054 | −0.0162 | −0.0027 |



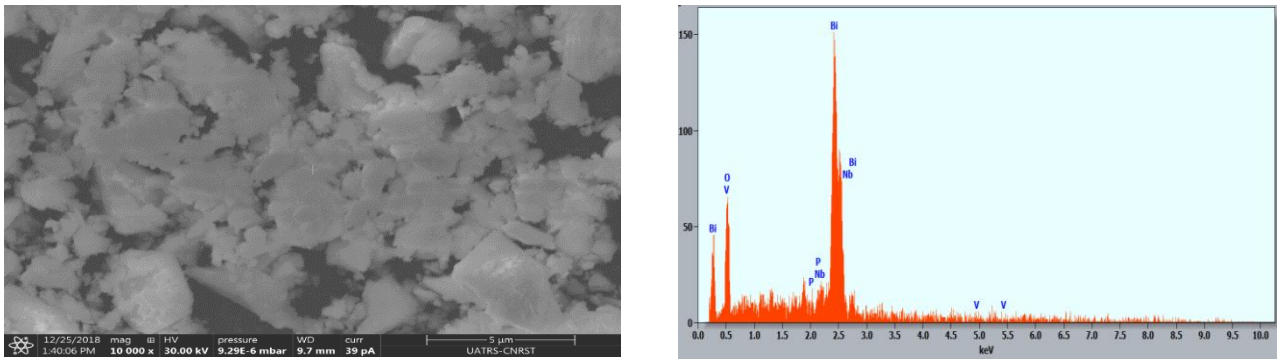

**$Bi_{17}Nb_3O_{33}$**




**$Bi_{17}Nb_{2.4}P_{0.3}V_{0.3}O_{33}$**




**$Bi_{17}Nb_{1.2}P_{0.9}V_{0.9}O_{33}$**




**$Bi_{17}Nb_{0.9}P_{1.05}V_{1.05}O_{33}$**

**Fig. 2.** SEM micrographs and corresponding EDX spectra for $Bi_{17}Nb_{3-4x}V_{2x}P_{2x}O_{33}$

The structural evolution described above — progressive lattice contraction with increasing local heterogeneity — provides the direct crystallographic basis for interpreting the optical behaviour discussed in the following section. Specifically, the average-structure contraction drives band-gap widening through enhanced orbital hybridisation, while the growing local structural disorder manifests optically as increasing Urbach energy. The two phenomena are therefore complementary and self-consistent descriptions of the same underlying compositional evolution.

### 3.2. Optical Properties and Band Gap Tuning

Both direct and indirect Tauc analyses were performed for comparison (**Fig. 3** and **Fig.4**). The indirect model (n = 1/2, **Fig. 3**) provides a superior linear fit in the band-edge region and is consistent with the reported indirect band structure of δ-$Bi_2O_3$ [18]; accordingly, the indirect Eg values are adopted throughout this work.

The optical behavior of $Bi_{17}Nb_{3-4x}V_{2x}P_{2x}O_{33}$ differs significantly from pure $Bi_{17}Nb_3O_{33}$, for which an indirect optical band gap of 1.76 eV was determined from **Fig. 3**. Upon introduction of pentavalent dopants, the absorption edge shifts toward higher energies. For $Bi_{17}Nb_{2.4}P_{0.3}V_{0.3}O_{33}$ (x = 0.15), the band gap increases to 2.13 eV, while $Bi_{17}Nb_{1.2}P_{0.9}V_{0.9}O_{33}$ (x = 0.45) and $Bi_{17}Nb_{0.9}P_{1.05}V_{1.05}O_{33}$ (x = 0.525) reach 2.18 eV and 2.16 eV, respectively.

The overall trend reflects the interplay between two competing contributions: a geometric effect, in which progressive lattice contraction enhances O 2p/Bi 6p orbital hybridisation and widens the fundamental gap; and an electronic effect, in which the progressive replacement of $Nb^{5+}$ ($4d^0$) by $V^{5+}$ ($3d^0$) partially lowers the conduction band minimum through the introduction of lower-energy V 3d states. The slight decrease in Eg from 2.18 eV (x = 0.45) to 2.16 eV (x = 0.525) is consistent with the V 3d contribution becoming increasingly significant at higher V loadings, partially offsetting the geometric widening. An additional contribution from band-tail broadening — as evidenced by the rising Urbach energy — may introduce a small systematic shift in the Tauc extrapolation at high dopant levels [18, 19].

The origin of the ~0.42 eV blue shift is multifactorial. Although the Burstein–Moss effect can occur in donor-doped oxides, the absence of carrier density measurements limits this interpretation [17]. Instead, systematic lattice contraction is proposed as the dominant driving force, though the partial replacement of $Nb^{5+}$ ($4d^0$) by $V^{5+}$ ($3d^0$) introduces a secondary

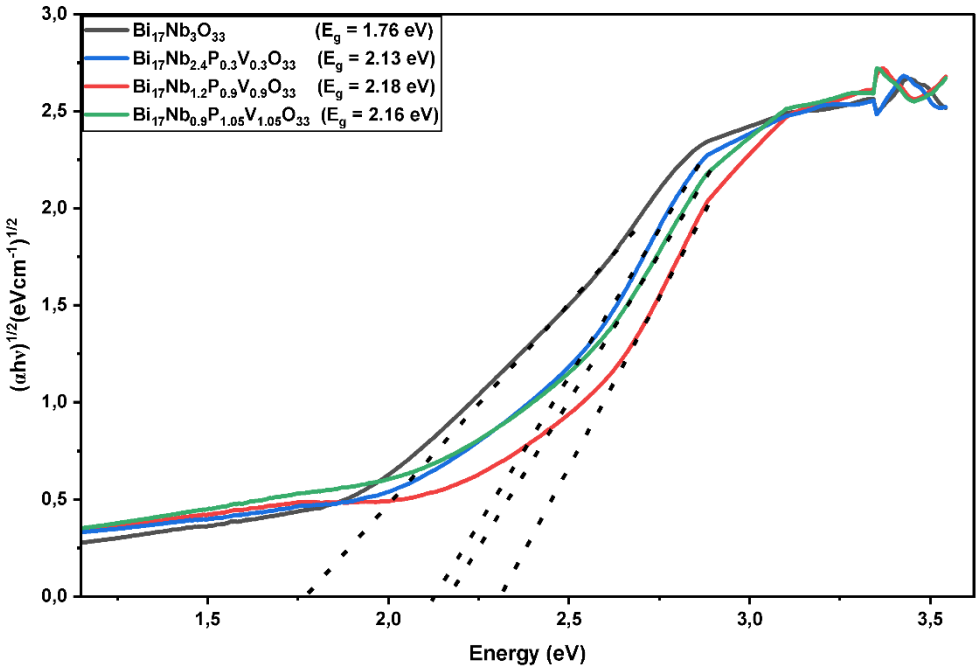



**Fig. 3.** Tauc plots of $(F(R_\infty)h\nu)^{1/2}$ versus photon energy ($h\nu$) used for the extraction of the indirect optical band gap ($E_g$) of the synthesized solid solutions

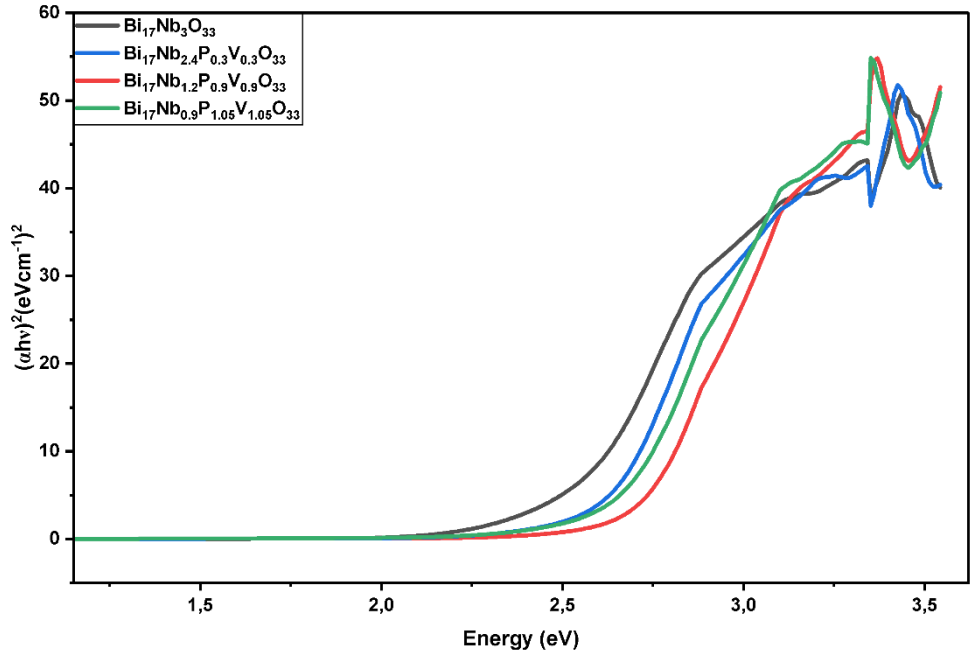



**Fig.4.** Tauc plots of $(F(R_\infty)h\nu)^2$ versus photon energy ($h\nu$) of the synthesized solid solutions

electronic contribution that modifies the conduction band minimum and accounts for the observed non-monotonic $E_g$ evolution across the series. Shorter Bi–O bond distances enhance the orbital overlap between O 2p states at the valence-band maximum and the Bi 6p (and, to a lesser extent, 6s) states at the conduction-band minimum, widening the fundamental gap through increased covalent hybridization. Additionally, the replacement of highly polarisable $Bi^{3+}$ ($6s^2$ lone pair) by the less polarisable pentavalent dopants modifies the local dielectric environment and reduces the excitonic binding contribution to the optical gap, providing a secondary contribution to the blue shift [26–33].

To quantify the structural disorder accompanying this blue shift, the Urbach energy ($E_u$) was evaluated from the linear region of the absorption tails using the exact derivative relation:

$$E_u = \left[\frac{d(lnF(R_\infty))}{d(h\nu)}\right]^{-1}$$

Eu increases from 280 meV ($Bi_{17}Nb_3O_{33}$) to 360 meV (x = 0.15), 350 meV (x = 0.45), and 410 meV (x = 0.525) (**Fig. 5**). The slight decrease from x = 0.15 to x = 0.45 — a difference of only 10 meV, which approaches the estimated uncertainty of the linear fitting procedure — may reflect partial strain compensation as the lattice adapts to a more homogeneously mixed multi-cation environment at intermediate compositions. The subsequent sharp rise to 410 meV at x = 0.525 indicates that the cumulative size mismatch, particularly from $P^{5+}$ (r = 0.38 Å for CN = 6), ultimately dominates and generates a higher density of band-tail localised states. Taken together, the overall increase in $E_u$ across the series confirms that multi-cation co-substitution introduces progressive structural disorder into the fluorite cation sublattice [13, 16, 34–36].

### 3.3. Theoretical Refractive Index Evaluation

Modification of the electronic band structure influences the optical constants of the material [37]. Based on the measured band gap values ($E_g$), the refractive index (n) was estimated using empirical relations proposed by Moss [32], Ravindra [30], and Hervé–Vandamme [34]:

**Moss Relation :** $n = \sqrt[4]{\frac{95}{E_g}}$

**Ravindra et al. Relation :** $n = 4.084 - 0.62(E_g)$

**Hervé–Vandamme Relation :** $n = \sqrt{1 + (\frac{13.6}{E_g + 3.4})^2}$

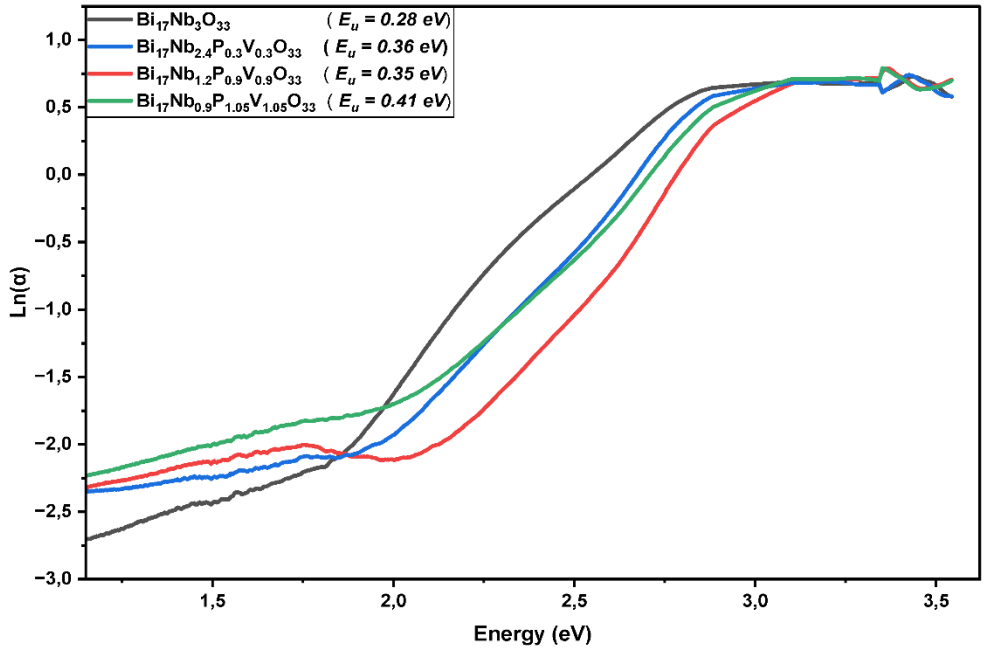



**Fig. 5.** Urbach plots of ln(F(R∞)) as a function of photon energy (hν) for the $Bi_{17}Nb_{3-4x}V_{2x}P_{2x}O_{33}$ solid solutions

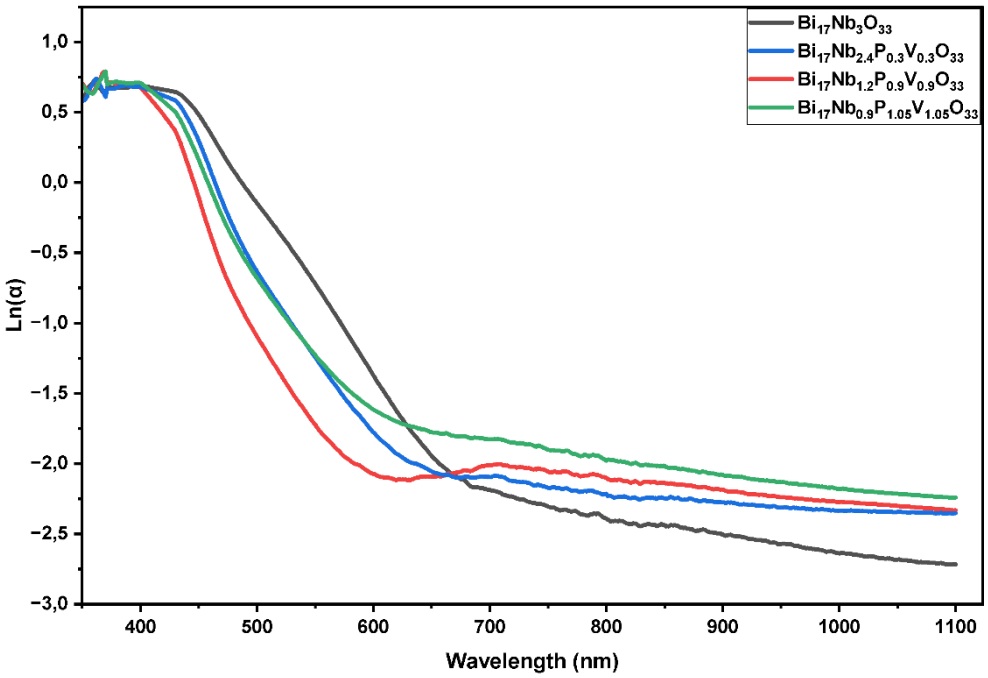



**Fig. 6:** Plot of ln(F(R∞)) as a function of wavelength for the $Bi_{17}Nb_{3-4x}V_{2x}P_{2x}O_{33}$ solid solutions

**Table 3**. Indirect Optical Band-Gap Energies ($E_g$) and Theoretically Estimated Refractive Indices (n) for the $Bi_{17}Nb_{3-4x}V_{2x}P_{2x}O_{33}$ Series

| Compound | $E_g$ (eV) | Refractive Index n | | |
|---|---|---|---|---|
| | | n(Moss ) | n(Ravindra) | n(Hervé–Vandamme) |
| $Bi_{17}Nb_3O_{33}$ | 1.76 | 2.71 | 2.99 | 2.82 |
| $Bi_{17}Nb_{2.4}P_{0.3}V_{0.3}O_{33}$ | 2.13 | 2.58 | 2.76 | 2.65 |
| $Bi_{17}Nb_{1.2}P_{0.9}V_{0.9}O_{33}$ | 2.18 | 2.57 | 2.73 | 2.63 |
| $Bi_{17}Nb_{0.9}P_{1.05}V_{1.05}O_{33}$ | 2.16 | 2.57 | 2.74 | 2.64 |

The estimated values are summarised in **Table 3**. Although these models were originally derived for classical semiconductors and should be regarded as first-order approximations for complex oxides, they are widely applied when experimental dispersion data (e.g., from spectroscopic ellipsometry) are unavailable. All three models yield a consistent and monotonically decreasing refractive index with increasing band gap, a trend well described by the Moss–Ravindra relation [38–42]. The reduction in n is attributed to the progressive replacement of the highly polarisable $Bi^{3+}$ cation (bearing a stereochemically active $6s^2$ lone pair) by the smaller, less polarisable pentavalent dopants, which reduces the electronic polarisability of the lattice and hence the high-frequency dielectric constant. These results suggest potential interest in these ceramics for dielectric coating applications, warranting future experimental verification of the optical dispersion by ellipsometry [43, 44].

## 4. Conclusion

In summary, $Bi_{17}Nb_{3-4x}V_{2x}P_{2x}O_{33}$ solid solutions (x = 0.15, 0.45, 0.525) were successfully synthesised by solid-state reaction, and the room-temperature stabilisation of the δ-$Bi_2O_3$-type cubic fluorite structure was confirmed by X-ray powder diffraction for all compositions. A systematic decrease in lattice parameter with increasing $V^{5+}/P^{5+}$ content was observed, consistent with Vegard's law and the smaller ionic radii of the pentavalent dopants relative to $Bi^{3+}$. Scanning electron microscopy revealed a dense, sintered morphology with polyhedral grain morphology. The observed band-gap widening of up to ~0.42 eV is attributed primarily to enhanced O 2p/Bi 6p orbital hybridisation driven by systematic lattice contraction, with a secondary contribution from the progressive modification of the conduction band minimum as V 3d states partially replace Nb 4d states with increasing x. The non-strictly-monotonic Eg evolution — reaching a maximum of 2.18 eV at x = 0.45 before decreasing slightly to 2.16 eV

at x = 0.525 — is consistent with this competing-mechanism interpretation. Although a Burstein–Moss contribution cannot be entirely excluded in donor-doped systems, its magnitude is expected to be negligible in the present stoichiometrically balanced compositions in the absence of experimental carrier-density data. The overall increase in Urbach energy from 280 to 410 meV across the series confirms growing structural disorder with increasing dopant loading, though the slight non-monotonicity observed at intermediate compositions (360 meV at x = 0.15, 350 meV at x = 0.45) suggests partial local strain compensation at balanced multi-cation occupancies. Empirical refractive index estimates reveal a correlated decrease in n with increasing $E_g$, consistent with classical polarisability arguments. Collectively, these results demonstrate that multi-cation Nb/V/P co-substitution is an effective strategy for engineering the optoelectronic properties of bismuth-based oxide ceramics, with potential relevance to visible-light photocatalysis and dielectric coating applications.

## Funding

The authors declare that no funds, grants, or other financial support were received from any organization during the preparation of this manuscript.

## References

[1] Harwig, H.A. Z. Anorg. Allg. Chem. 444, 151–166 (1978).

[2] Boivin, J.C., Mairesse, G. Chem. Mater. 10, 2870–2888 (1998).

[3] Sammes, N.M., Tompsett, G.A., Näfe, H., Aldinger, F. J. Eur. Ceram. Soc. 19, 1801–1826 (1999).

[4] Shuk, P., Wiemhöfer, H.D., Guth, U., Göpel, W., Greenblatt, M. Solid State Ionics 89, 179–196 (1996).

[5] Takahashi, T., Iwahara, H. Mater. Res. Bull. 13, 1447–1453 (1978).

[6] Takahashi, T., Iwahara, H., Esaka, T. J. Electrochem. Soc. 124, 1563–1569 (1977).

[7] Fung, K.Z., Virkar, A.V. J. Am. Ceram. Soc. 74, 1970–1980 (1991).

[8] Valant, M., Suvorov, D. Chem. Mater. 13, 353–359 (2001).

[9] Firman, K., Tan, K.B., Khaw, C.C., Zainal, Z., Tan, Y.P., Chen, S.K. J. Mater. Sci. 52, 10106–10118 (2017).

[10] Jie, Y.C., Eysel, W. Powder Diffr. 10, 76–80 (1995).

[11] Baach, B., Boudad, L., Saber, I., Taibi, M.H., Guedira, T. Mater. Chem. Phys. 317, 129201 (2024).

[12] Pirnat, U., Valant, M., Jančar, B., Suvorov, D. Chem. Mater. 17, 5155–5160 (2005).

[13] Urbach, F. Phys. Rev. 92, 1324 (1953).

[14] Cody, G.D. Semicond. Semimetals 21, 11–82 (1984).

[15] Hamberg, I., Granqvist, C.G., Berggren, K.F., Sernelius, B.E., Engström, L. Phys. Rev. B 30, 3240 (1984).

[16] Mistonov, A.A., Chumakov, A.P., Ermakov, R.P., Iskhakova, L.D., Zakharova, A.V., Chumakova, A.V., Kvashnina, K.O. J. Alloys Compd. 753, 646–654 (2018).

[17] Shannon, R.D. Acta Crystallogr. A 32, 751–767 (1976).

[18] Omari, L.H., Hajji, L., Haddad, M., Lamhasni, T., Jama, C. Mater. Chem. Phys. 223, 60–67 (2019).

[19] Walsh, A., Watson, G.W., Payne, D.J., Edgell, R.G., Guo, J., Glans, P.A., et al. Phys. Rev. B 73, 235104 (2006).

[20] Zhou, W. J. Solid State Chem. 108, 265–276 (1994).

[21] International Centre for Diffraction Data (ICDD), PDF 27-0052, δ-$Bi_2O_3$ reference pattern.

[22] Sanna, S., Esposito, V., Andreasen, J.W., Hjelm, J., Zhang, W., Kasama, T., et al. Nat. Mater. 14, 500–504 (2015).

[23] Vegard, L. Z. Phys. 5, 17–26 (1921).

[24] Singh, S.A., Madras, G. Sep. Purif. Technol. 105, 79–89 (2013).

[25] Withers, R.L., Ling, C.D., Schmid, S. Z. Kristallogr. 214, 296–304 (1999).

[26] Burstein, E. Phys. Rev. 93, 632–633 (1954).

[27] Moss, T.S. Proc. Phys. Soc. B 67, 775 (1954).

[28] Tuyikeze, V., Omari, L.H., Bouhbou, M., Boudali, A., Fraija, F. Mater. Today Proc. 30, 828–832 (2020).

[29] Gupta, V.P., Ravindra, N.M. Phys. Status Solidi B 100, 715 (1980).

[30] Ravindra, N.M., Srivastava, V.K. Infrared Phys. 21, 283–285 (1981).

[31] Wemple, S.H., DiDomenico Jr., M. Phys. Rev. B 3, 1338–1351 (1971).

[32] Moss, T.S. Proc. Phys. Soc. B 63, 167–176 (1950).

[33] Ravindra, N.M., Auluck, S., Srivastava, V.K. Phys. Status Solidi B 93, K155–K160 (1979).

[34] Hervé, P., Vandamme, L.K.J. Infrared Phys. Technol. 35, 609–615 (1994).

[35] Lamichhane, A. Solids 4, 316–326 (2023).

[36] Balci, M. J. Aust. Ceram. Soc. 60, 385–397 (2024).

[37] Katubi, K.M., et al. Opt. Quantum Electron. 56, 625 (2024).

[38] Islam, A., et al. arXiv arXiv:2404.04768 (2024).

[39] Depero, L.E. J. Solid State Chem. 122, 439–443 (1996).

[40] Ling, C.D. J. Solid State Chem. 158, 34–49 (2001).

[41] John, S., Soukoulis, C., Cohen, M.H., Economou, E.N. Phys. Rev. Lett. 57, 1777 (1986).

[42] Balci, M., et al. Res. Square (preprint) (2024).

[43] Bouderbala, I.Y., et al. Appl. Phys. A 130, 205 (2024).

[44] Alsaiari, N.S., Umer, R., Basha, B., Boukhris, I., Alsafari, I.A., Al-Buriahi, M.S., et al. J. Taibah Univ. Sci. 19, 2596383 (2025).